Microstructure, corrosion behavior and cytotoxicity of Zr–Nb alloys for biomedical application

F.Y. Zhou [a], B.L. Wang [a], K.J. Qiu [a], W.J. Lin [a], L. Li [a], Y.B. Wang [b], F.L. Nie [b], Y.F. Zheng [a,b,*]

[a] Center for Biomedical Materials and Engineering, Harbin Engineering University, Harbin 150001, China
[b] Department of Materials Science and Engineering, College of Engineering, Peking University, Beijing, China

ARTICLE INFO

ABSTRACT

In this work, the effects of Nb content on microstructure and corrosion behaviors of biomedical Zr–Nb alloys were systematically studied. The results of XRD analysis and optical microscopy indicated that the experimental Zr–Nb alloys had a duplex structure of α and β phases, and the content of β phase increased with the increase of Nb content. The electrochemical impedance spectroscopy (EIS) studies showed an improvement on the resistance of the spontaneous oxide film with increasing Nb content. The EIS data, fitted by $R_s(Q_pR_p)$ model, suggested a single passive film formed on the experimental material surfaces. Polarization tests in Hank's solution revealed a nobler electrochemical behavior of the Zr–Nb alloys after alloying Nb to pure Zr. The corrosion resistance increased with increasing Nb content, as indicated by lower corrosion current densities and passive current densities and higher pitting potentials. The major components on the surfaces of the corroded Zr–Nb alloy samples detected by XPS were ZrO_2 and Nb_2O_5. The biocompatibility of Zr–Nb alloys was primarily evaluated by culturing L-929 cells in the extraction media of Zr–Nb alloy samples and excellent results were obtained. All of these above results suggested that the Zr–22Nb alloy, among the experimental alloys, showed a promising potential for biomedical applications.

© 2012 Elsevier B.V. All rights reserved.

1. Introduction

Due to their acceptable mechanical strength and good biocompatibility as well as superior corrosion resistance, zirconium (Zr) and its alloys have become a candidate for surgical implants [1,2]. Zr has been proved to be nontoxic and biocompatible [3,4]. In vivo animal experiments showed that zirconium implants exhibited good osseointegration [5] and even a higher contact degree than titanium implants for bone–implant interface [6]. Oxinium (surface oxidized Zr–2.5Nb alloy) has been successfully used as an articulating head material in total knee replacement (TKR) and total hip replacement (THR) surgeries because of its superior wear performance against UHMWPE in relation to the traditional head materials such as Co–Cr alloys [7,8].

Some new biomedical Zr-based alloys have been designed and investigated by choosing the biocompatible elements for alloying of pure Zr, such as Zr–xTi alloys [9] and Zr–xMo alloys [10]. Besides, surface modifications were employed to improve the biochemical properties of the substrate. In M. Uchida's study [11], the apatite-forming ability of NaOH-treated zirconium metal in SBF was investigated and it was found that the Zr–OH group of the zirconia gel induced apatite nucleation. In addition, the formation of ZrO_2 nanotubes was investigated and discussed [12]. Furthermore, a recent study on ultra-fine grained (UFG) Zr obtained by severe plastic deformation (SPD) showed improved mechanical properties together with excellent in vitro biocompatibility, which made UFG Zr a promising biomaterial for surgical implants [13].

The spontaneous formation of a thin oxide film on surfaces of Zr and its alloys in electrolytes offers them superior corrosion resistance [14–16]. However, the passive film is not very stable and pits easily occur for Zr and Zr alloys in chloride medium [15,17]. Nb is a major alloying element for Zr and the microstructure is much affected by the Nb content [18]. The tensile strength of solution-treated Zr–xNb alloys increased proportionally with Nb content [19]. In addition, Zr–20Nb alloy showed relatively a good balance of tensile strength and elongation, and a low Young's modulus (around 58 MPa). Nevertheless, there are only a few investigations on microstructure and corrosion behaviors of Zr–Nb alloys with a higher Nb content. The electrochemical and morphological characterizations of anodic oxide films on biomedical Zr–Nb alloys were rarely carried out. Therefore, it is very important to investigate the composition of the passive films on various Zr–Nb alloys, which may be helpful to understand the corrosion mechanism in physiological solution. Based on the information from binary Nb–Zr phase diagram [20], 18.8 wt.% Nb could be recognized as the maximum solubility in β-Zr phase. In this paper, Zr–Nb alloys with 16 wt.% Nb (<18.8 wt.%) and 22 wt.%

* Corresponding author at: Department of Materials Science and Engineering, College of Engineering, Peking University, Beijing 100871, China. Tel./fax: +86 10 6276 7411.
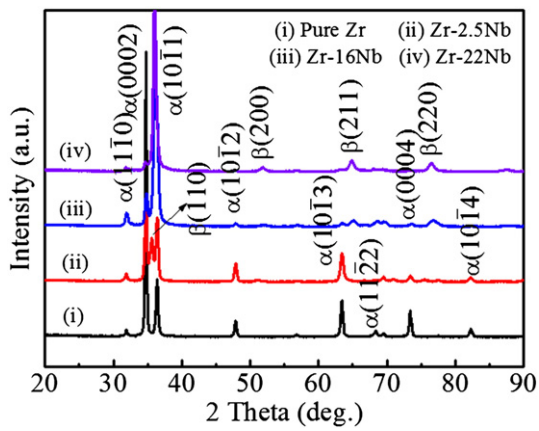E-mail address: yfzheng@pku.edu.cn (Y.F. Zheng).

Fig. 1. XRD profiles of pure Zr and Zr–Nb alloys at room temperature.

Nb (>18.8 wt.%) contents associated with Zr–2.5Nb alloy were chosen and investigated. The goal of this work was to clarify the influence of the increase of Nb content on microstructure, in vitro corrosion behaviors and biocompatibility of these Zr–Nb alloys. For a better understanding of the effect of Nb content on corrosion resistance in simulated physiological media, the morphological and chemical characterizations of the passive films on various Zr–Nb alloys were performed, since stability of the passive film is directly associated with its biocompatibility for a biomedical metal material.

2. Experimental

2.1. Material preparation

The binary Zr–Nb alloys with the addition of 2.5, 16 and 22 wt.% Nb, were made in a vacuum arc-melting furnace under an Ar atmosphere using Zr wire (99.99%) and Nb wire (99.99%) as the raw materials. Each ingot was melted six times for promoting the homogeneity of the alloying element, and these ingots were hot-rolled to ~1.5 mm thick sheets at 800 °C. Finally, the hot-rolled plates were annealed at 500 °C for 1 h.

2.2. Structure characterization

Phase identification was performed by X-ray diffraction (XRD) at room temperature, using the Cu Kα radiation at 35 kV and 20 mA. The microstructures of the experimental alloys were examined by an optical microscope. The samples were mechanically polished via a standard metallographic procedure and then etched in a solution composed of 10% HF, 40% HNO_3 and 50% H_2O in volume.

2.3. Electrochemical corrosion measurement

Electrochemical experiments were conducted using a CHI660 electrochemical workstation and a three-electrode system was employed which was composed of a platinum foil, an Ag/AgCl electrode as a counter and a reference electrode. Working electrolyte was Hank's physiological solution with pH value 7.4 [14]. Prior to immersion, the tested samples were wetly ground with water-proof SiC papers to 2000 grit. Finally they were cleaned in acetone, ethanol and deionized water in an ultrasonic bath. All experiments were carried out at 37 °C in a water bath.

The open-circuit potential (OCP) measurements were carried out on freshly cleaned samples and maintained up to 5400 s. Electrochemical impedance spectroscopy (EIS) measurements were carried out at OCP, by applying a sinusoidal potential perturbation of 10 mV with frequency sweep from 10 kHz to 0.01 Hz. The impedance data were analyzed and fitted to appropriate equivalent electrical circuit using the ZSimpWin3.21 software. The potentiodynamic polarization measurement was conducted from −0.8 V to 1.5 V (vs. Ag/AgCl) at a scan rate of 1 mV/s.

X-ray photoemission (XPS) analysis was performed with an Axis Ultra spectrometer using mono Al Kα radiation at vacuum pressure of 10^{-9} bar, 15 kV and 15 mA. The binding energy was calibrated
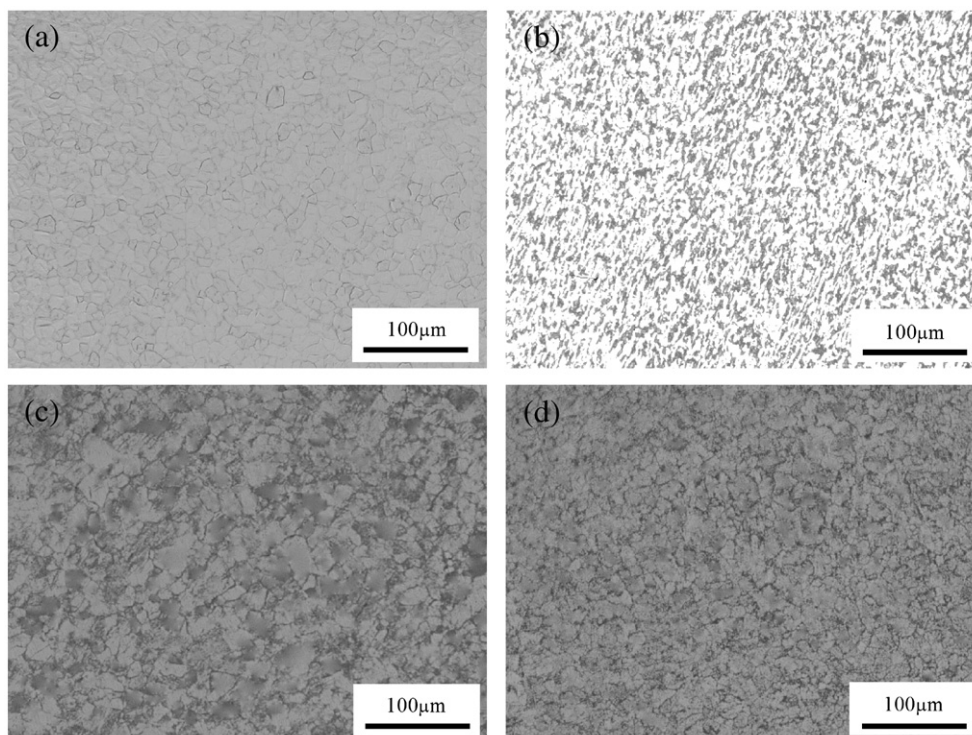

Fig. 2. Optical micrographs of (a) pure Zr, (b) Zr–2.5Nb, (c) Zr–16Nb and (d) Zr–22Nb alloy samples.
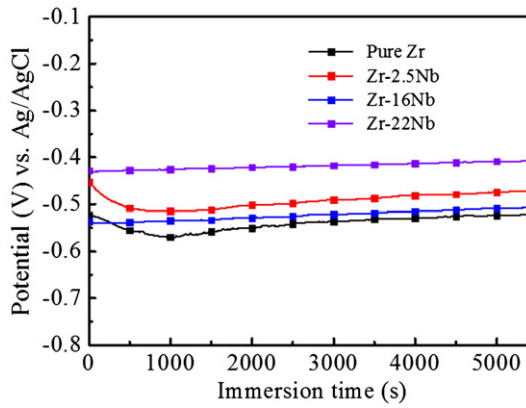
Fig. 3. Open-circuit potential vs. time curves of pure Zr and Zr–Nb alloys in Hank's solution.

using C 1s hydrocarbon peak at 284.8 eV. Samples were cleaned by sputtering with argon ion gun for 300 s. The morphology of the corroded samples was examined by scanning electron microscopy (SEM).

2.4. Cytotoxicity test

The cytotoxicity tests were carried out in an indirect way according to ISO 10993–5:1999 [21]. Before the test, all the samples were polished with water-proof SiC paper to 2000 grit. The cells chosen to evaluate the cytotoxicity of pure Zr and Zr–Nb alloys were fibroblast cells (L-929). Firstly, these cells were cultured in Dulbecco's modified Eagle's medium (DMEM) containing 10% fetal bovine serum (FBS), 100 U/ml penicillin and 100 μg/ml streptomycin in an incubator at

Table 1
Fitted parameters obtained using the $R_s(Q_pR_p)$ model to fit the experimental EIS data for pure Zr and various Zr–Nb alloys.

Materials	R_s ($\Omega \cdot cm^2$)	Q_p ($\mu F \cdot cm^{-2} \cdot s^{n-1}$)	n	R_p ($\times 10^5 \Omega \cdot cm^2$)	χ^2 ($\times 10^{-4}$)
Pure Zr	28.13	14.53	0.9345	1.69	6.10
Zr-2.5Nb	33.52	10.49	0.9398	2.82	11.10
Zr-16Nb	33.97	12.55	0.9137	4.64	10.44
Zr-22Nb	35.06	9.43	0.9285	5.15	10.95

37 °C in a humidified atmosphere with 5% CO_2. Extracts were obtained using DMEM serum free medium as the extraction medium. For each 1.25 cm^2 of material, 1 ml of culture medium was used and then incubated for 72 h. The supernatant fluid was withdrawn and centrifuged to prepare the extraction medium for the cytotoxicity test. In all tests the DMEM medium was used as a negative control, and DMEM medium containing 0.64% phenol as a positive control. Cells were seeded in 96-well cell culture plates at a density of 5×10^3 cells/100 μl medium in each well and incubated for 24 h to allow attachment. Then, the medium was substituted by 100 μl extracts obtained from the materials. After incubating the cells in a humidified atmosphere with 5% CO_2 at 37 °C for 48 and 96 h, respectively, the 96-well cell culture plates were observed under an optical microscope. After that, 10 μl MTT was added to each well, followed by 4 h incubation at 37 °C in darkness. Then 100 μl formazan solubilization solution (10% SDS in 0.01 M HCl) was added in each well overnight in the incubator. The spectrophotometrical absorbance of the samples was measured by microplate reader (Bio-RAD680) at 570 nm with a reference wavelength of 630 nm.

3. Results

3.1. Microstructures

Fig. 1 presents the XRD profiles of pure Zr and Zr–Nb alloys. For Zr–2.5Nb sample, β phase (body centered cubic) in the form of (211) peak was visible in addition to the peaks from α phase (hexagonal close packed). Both Zr–16Nb alloy and Zr–22Nb alloy consisted of duplex phases, α and β. However, it was noteworthy that β peaks showed higher intensities in the sequence of Zr–2.5Nb, Zr–16Nb and Zr–22Nb alloys. The obtained results indicated that β phase increased with the increase of Nb content.

Fig. 2 shows optical micrographs of pure Zr and Zr–Nb alloys. An equiaxed grain structure was observed for pure Zr. The microstructure of the studied Zr–Nb alloys varied with the different amounts of Nb contents. The annealed Zr–2.5Nb alloy had a typical duplex microstructure which contained 2nd phase (dark) in a matrix of α phase
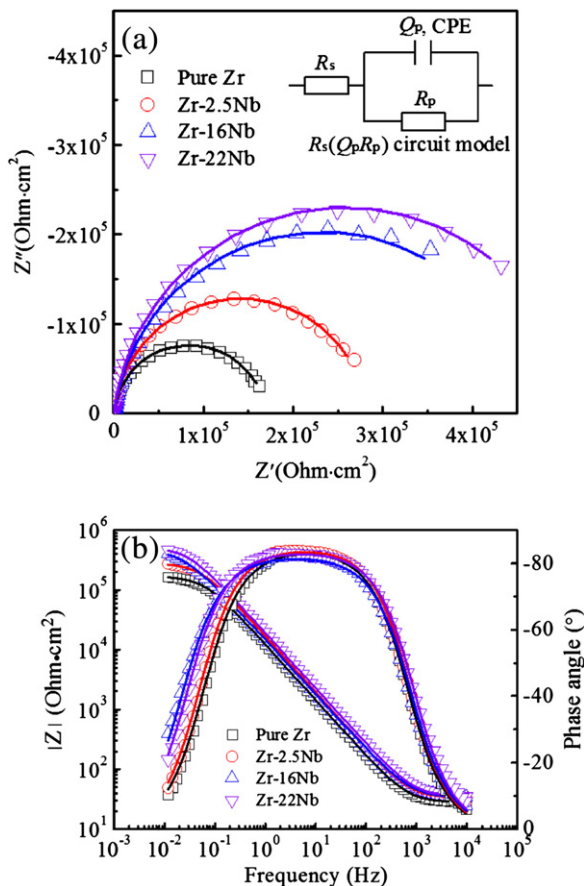

Fig. 4. Electrochemical impedance spectra of pure Zr and Zr–Nb alloys: (a) Nyquist plots and (b) Bode plots (line: fitted data; symbol: experimental data).
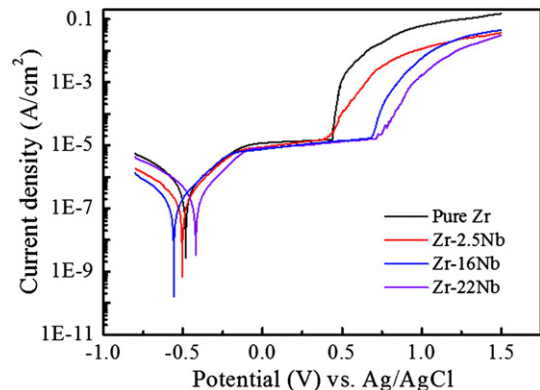

Fig. 5. Potentiodynamic polarization curves of pure Zr and Zr–Nb alloys in Hank's solution.

Table 2
Corrosion parameters of pure Zr and Zr–Nb alloys obtained from polarization curves.

Materials	E_{corr} (V)	I_{corr} ($\mu A/cm^2$)	I_{pass} ($\mu A/cm^2$) at different potentials (V)			E_{tran} (V)
			0	0.3	0.5	
Pure Zr	−0.491 ± 0.109	0.529 ± 0.185	7.84 ± 3.55	15.28 ± 1.02	–	0.402 ± 0.128
Zr–2.5Nb	−0.500 ± 0.007	0.472 ± 0.054	7.35 ± 0.97	11.65 ± 2.74	–	0.376 ± 0.017
Zr–16Nb	−0.531 ± 0.037	0.312 ± 0.081	7.45 ± 1.45	11.57 ± 1.32	14.00 ± 1.44	0.660 ± 0.036
Zr–22Nb	−0.439 ± 0.042	0.349 ± 0.082	6.38 ± 1.69	9.97 ± 0.48	12.73 ± 0.69	0.728 ± 0.065

(light). For Zr–16Nb and Zr–22Nb alloy samples, equiaxial polygonal grains were observed and the size of grains for Zr–22Nb alloy seemed to be smaller than that of Zr–16Nb alloy.

3.2. Open-circuit potential (OCP)

Fig. 3 shows OCP vs. time curves of pure Zr and experimental Zr–Nb alloys in Hank's solution. It was found that the profiles of OCP for pure Zr and Zr–2.5Nb alloys were quite similar. The potentials became more negative in the initial stage and then increased towards the more positive direction with increasing time. For Zr–16Nb and Zr–22Nb alloys, OCPs changed slowly towards noble potentials during the whole immersion time. This fact implied that pure Zr and the studied Zr–Nb alloys spontaneously formed passive films on the metallic surfaces in Hank's solution. The final OCP values of pure Zr, Zr–2.5Nb, Zr–16Nb and Zr–22Nb alloy samples were −0.521 V, −0.472 V, −0.507 V and −0.408 V, respectively.

3.3. Electrochemical impedance spectroscopy (EIS)

Fig. 4 shows the EIS results, in the form of the Nyquist plots and the Bode plots, after 1.5 h immersion to reach a stable state in Hank's solution. As the Nyquist plots showed, it was obvious that all the Nyquist plots in the impedance spectra were characterized by a large partial semicircle and the diameter of the semicircle increased with the increasing Nb content during the same immersion time,

which indicated a nobler electrochemical characteristic with the addition of Nb and the increase of its content [22]. From the Bode plots between log |Z| and log f, it could be observed that the curves were composed of a flat portion in the high frequency (1–10 kHz), which was due to the resistance of electrolyte, and a linear variation at a wide range of frequencies, with a slope close to −1, indicating a response of a capacitive behavior of passive film [23,24]. The Bode-phase angle plots displayed a near-capacitive response with a phase angle about −80° in the middle-frequency ranges indicating a typical passive film present on the surface [23,24].

In the present paper, an equivalent circuit model $R_s(Q_pR_p)$ (shown in Fig. 4(a)) with only a one time constant was employed to fit the EIS data in the case of a single passive film formed on the metal surface [23–25]. The parameters R_s and R_p represented electrolyte resistance and the resistance of passive film, respectively. Q_p was a constant phase element (CPE), which took into account the non-ideal capacitive behavior of the film. Values of fitted parameters (R_s, Q_p, n, and R_p) are listed in Table 1. The good agreement between the experimental data and fitted data was obtained with the χ^2 of about 10^{-3}. The values of the passive film resistance (R_p) became larger with an increase of Nb content.

The above impedance results suggested that the addition of Nb element was beneficial for increasing the resistance of the passive film of the Zr-based alloys. Zr–22Nb alloy had higher corrosion resistance than other Zr–Nb alloys studied at 1.5 h immersion in Hank's solution.
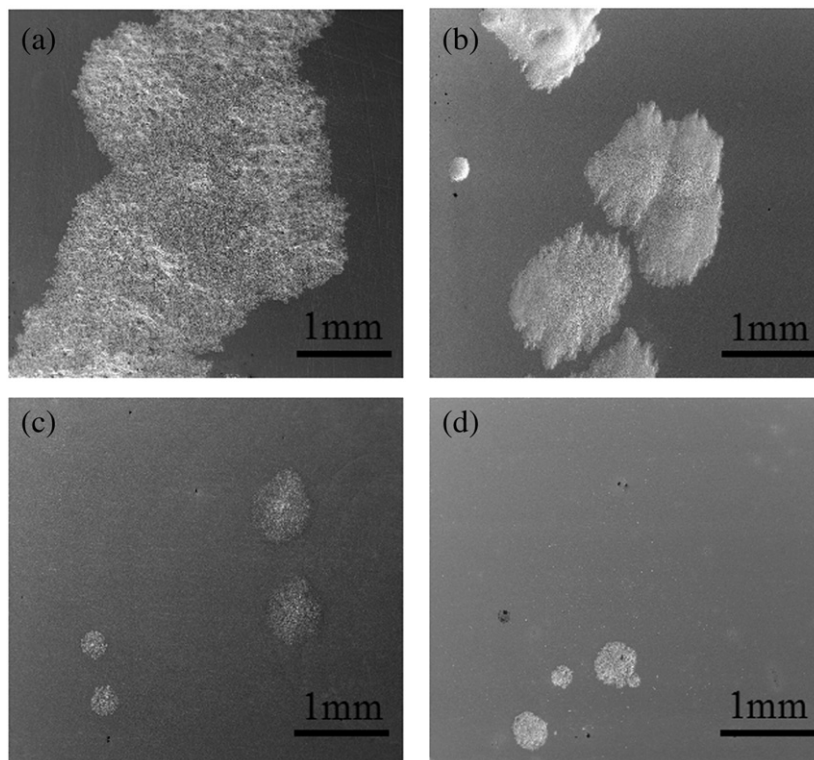
Fig. 6. SEM micrographs of (a) pure Zr, (b) Zr–2.5Nb alloy, (c) Zr–16Nb alloy and (d) Zr–22Nb alloy surfaces after potentiodynamic polarization in Hank's solution.

3.4. Potentiodynamic polarization

The potentiodynamic polarization curves of pure Zr and Zr–Nb alloys in Hank's solution are given in Fig. 5. The test samples showed quite similar polarization behaviors with the increasing potential. They were passivated and showed the passive regions before the protective films were broken. These data were similar to the experimental results obtained by Branzoi et al. [14] for Zr–Nb, Zr–Ta and Zr–Nb–Ta alloys. The average values E_{corr} and I_{corr} from polarization curves calculated by CorrView software are presented in Table 2. The average I_{corr} values of all the test samples were 0.529, 0.472, 0.312 and 0.349 (in $\mu A/cm^2$) for pure Zr, Zr–2.5Nb, Zr–16Nb and Zr–22Nb alloys, respectively. It could be seen that the corrosion resistance of Zr–Nb alloys improved after alloying Nb to pure Zr regardless of the Nb contents.

A passive region was observed on the anodic polarization curves before transpassivation occurrence, which indicated that the stable and protective films formed on the surface of the samples. The passive current densities obtained at different potentials during the passive range are given in Table 2. The anodic current densities of all test
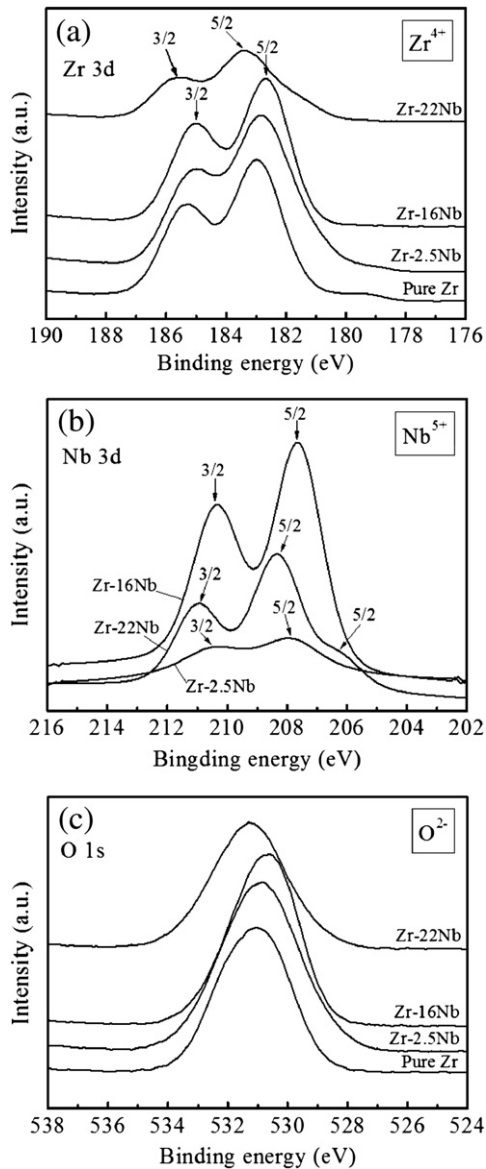
Table 3
Composition of the corroded surfaces for pure Zr and Zr–Nb alloys estimated using XPS analysis.

Materials	Content (mol%)		
	Zr	Nb	O
Pure Zr	24.95	0	75.05
Zr–2.5Nb	23.76	0.32	75.92
Zr–16Nb	21.79	3.48	74.73
Zr–22Nb	20.65	3.97	75.38

alloy samples were around 5–15 $\mu A/cm^2$ and their values decreased from Zr–2.5Nb alloy to Zr–22Nb alloy. It suggested that a more stable passive oxide film formed on the samples' surface of Zr–Nb alloys with the increase of Nb content. At more positive potentials, the passive films broke down and the current densities increased rapidly. The breakdown potentials for pure Zr and Zr–Nb alloys are listed in Table 2. Compared with pure Zr, the breakdown potential for Zr–2.5Nb alloy decreased slightly, while that of Zr–16Nb and Zr–22Nb alloys increased up to 0.66 V and 0.728 V in average, respectively. Hence, the addition of more alloying element Nb led to the increase of the stability of passive films and, consequently, the corrosion resistance increase for these biomedical Zr–Nb alloys in Hank's solution.

3.5. Surface analyses

The surface morphology of samples after pit corrosion is shown in Fig. 6. In general, randomly distributed pitting spots were present on the sample surfaces, which confirmed the pits' occurrence. For Zr–2.5Nb alloy, spots existed in a smaller area than in the case of pure Zr. Compared with those on pure Zr and Zr–2.5Nb alloy samples, the extents detected on the surfaces of Zr–16Nb and Zr–22Nb alloys were much smaller. This confirmed the evidence that the Zr–Nb alloys became more pit-resistant with the increase of Nb content.

XPS spectra from pure Zr and Zr–Nb alloys after corrosion are given in Fig. 7. The Zr 3d spectra consisted of $3d_{5/2}$ and $3d_{3/2}$ electron peaks that were assigned to Zr^{4+} oxide state [26,27]. Nb 3d spectra exhibited a similar profile with $3d_{5/2}$ and $3d_{3/2}$ corresponding to Nb^{5+} oxide state [26]. The peaks at binding energy region of 531.0–531.3 eV in O 1s spectra were assigned to O^{2-} oxide state [27]. Thus, the major components on the surfaces of the corroded Zr–Nb alloy samples were protective ZrO_2 and Nb_2O_5. The composition for each element on the surface of pure Zr and various Zr–Nb alloys is listed in Table 3. It could be observed that the Nb content of the
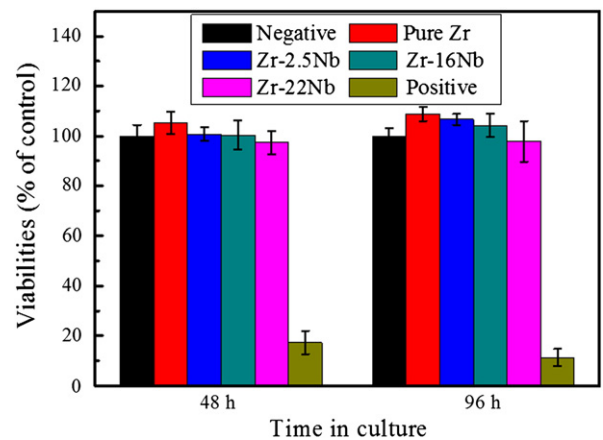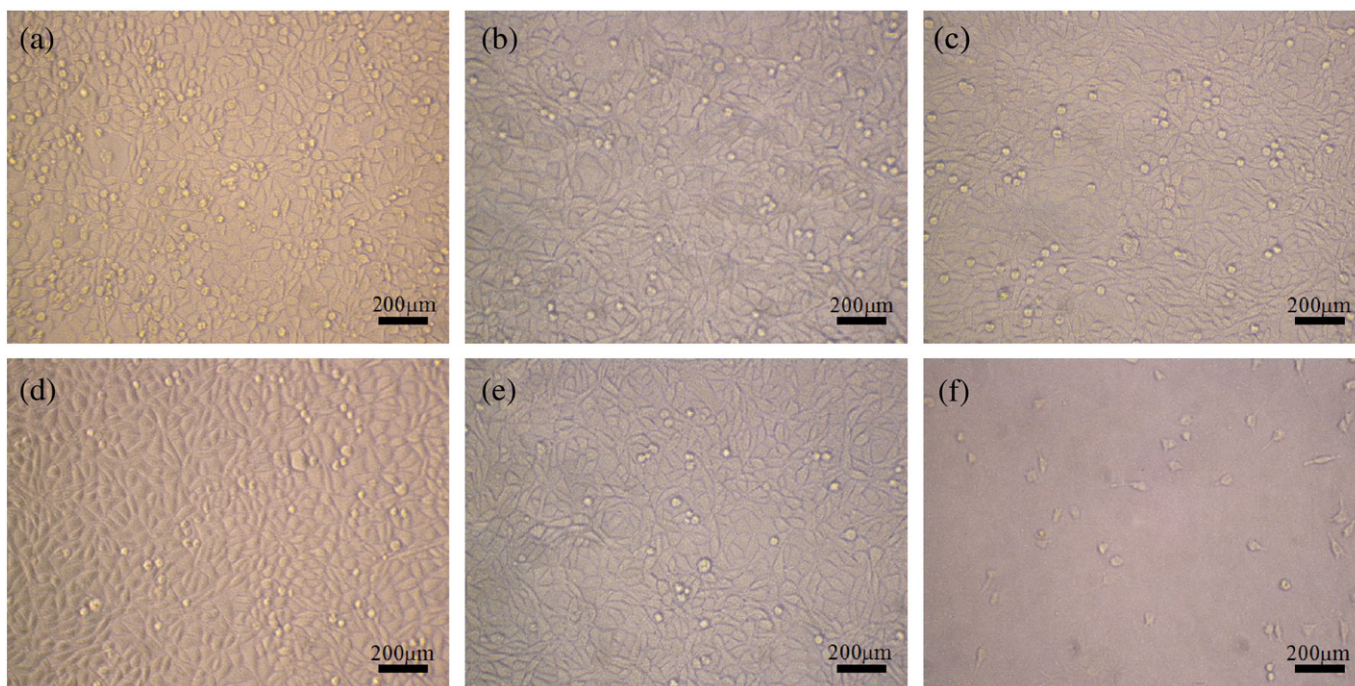

Fig. 7. XPS spectra of (a) Zr 3d, (b) Nb 3d, and (c) O 1s for pure Zr and Zr–Nb alloys after potentiodynamic polarization in Hank's solution.

Fig. 8. Cell viability of L-929 after 48 and 96 h of culture in pure Zr and Zr–Nb alloy extraction media.

Fig. 9. Optical images of L-929 cells after 96 h of culture in pure Zr and Zr–Nb alloy extraction media: (a) negative control, (b) pure Zr, (c) Zr–2.5Nb alloy, (d) Zr–16Nb alloy, (e) Zr–22Nb alloy and (f) positive control.

oxide films on the surfaces increased from Zr–2.5Nb alloy to Zr–22Nb alloy in sequence.

3.6. Evaluation of cytotoxicity

Fig. 8 shows the viability of the fibroblast cells (L-929) expressed as a percentage of the viability of cells grown in the negative control after culturing in pure Zr and Zr–Nb alloy extraction media for different periods (48 and 96 h). It could be seen that the cell viability of studied Zr–Nb alloys was almost the same as that of the negative group and slightly lower than that of pure Zr after 48 h of culture. The cell viability in every sample extract increased with the culture period, although cell viability decreased with the increase of Nb content after 96 h of culture. Therefore, the results indicated that, after alloying Nb to pure Zr, the extracts of Zr–Nb alloys had little influence on the cell growth and proliferation. Fig. 9 illustrates the results of morphological observations of L-929 cells culturing in pure Zr and Zr–Nb alloy extracts for 96 h. A confluent cell monolayer showing the typical spindle-shaped morphology was observed in the negative group and in the case of all Zr–Nb alloy extracts. In contrast, much fewer cells were found in the positive group. Thus, the studied Zr–Nb alloys were judged to be in vitro biocompatible.

4. Discussion

Nb was the β-stabilizer for Zr alloys and over 20% concentration β phase could be fully retained by quenching from the β phase field [28]. The study of Woo and Lin [29] on a Zr–20Nb alloy implied that single β phase was obtained by vacuum annealing at 850 °C for 1 h and air-cooled. In the present paper, Zr–Nb alloys with various Nb contents consisted of α and β (β-Zr) phases after being hot rolled at 800 °C and being annealed at 500 °C for 1 h. For Zr–2.5Nb alloy, the β phases were discontinuous and were separated with α phase units, which was similar to other experimental results [18]. It was difficult to clearly distinguish between α and β grains according to the optical micrographs for Zr–16Nb and Zr–22Nb alloys. Combined with XRD results, these Zr–Nb alloys with higher Nb contents exhibited two-phase constitution and the volume fraction of β phase

increased with increasing Nb content, which was consistent with the law of phase diagrams.

The general conclusion of the electrochemical corrosion studies was that addition of Nb improved the corrosion resistance of pure Zr, and with the increase of Nb content for Zr–Nb alloys, the corrosion resistance increased and the oxide films became more stable. Pitting occurred at a more positive potential for pure Zr and all studied Zr–Nb alloys. The corrosion performances of Zr and its alloys depended largely on factors such as composition, environment and structure. The corrosion studies carried out on various alloys clearly indicated that when adding Ti, Nb, and Ta to pure Zr, its corrosion performance improved and Hf lowered its corrosion resistance [14,16,30]. In addition, the growth and stability of the oxide films on Zr and its alloys were much affected by electrolytic medium. Their corrosion properties were deteriorated with the presence of chloride ions [17,31]. The passive films were easily attacked due to the Cl^- migration towards and into the oxide films, which caused pitting. Oliveira et al. [15] found out that the pitting potential of Zr–50 at.% Ti alloy was much higher in Na_2SO_4 solution (Cl^- free) compared with that in Ringer's solution (Cl^- containing). Palit and Elayaperumal [32] had discussed that the pitting resistance of Nb was greater than that of Zr in Cl^- containing solution. It was reasonably inferred that Nb-oxide was more compact and stable. This may account for improvement on corrosion resistance for pure Zr with addition of Nb. In addition, increased corrosion resistance was expected with the increasing Nb content, because Nb_2O_5 content of the oxide films on the surface was higher in this case. It is necessary for the implanted metals or alloys to remain at the passive state. Therefore, the broken potentials of implants are required to be higher than the body potential. It was suggested that the body potential corresponded to the redox potential of the body fluid with a value of 0.4–0.5 V [3]. In this study, the broken potentials of Zr–16Nb alloy and Zr–22Nb alloy were 0.66 V and 0.728 V in average, higher than that of 316 L stainless steel implant [3], showing a promising potential for new implants.

The cytotoxicity testing is widely used to evaluate the biocompatibility of biomaterials in vitro [33]. The biocompatibility of Zr and Nb was demonstrated as excellent by in vitro metal ion cytotoxicity tests [34] and in vivo tests [3]. In comparison with the traditional

implant alloys such as stainless steel (containing Ni), Co–Cr–Mo and Ti–6Al–4V, Zr and Nb showed less toxicity than Ni, Co and V [35]. In addition, the excellent biocompatibility was related to the formation of biocompatible oxides, such as ZrO_2 and Nb_2O_5 [3,36]. The stable oxides could effectively inhibit the release of metal ions and these metal oxides themselves showed inertness, low solubility and high negative heat of mixing, indicating good biocompatibility [36,37].

5. Conclusions

The microstructure and electrochemical corrosion together with cytotoxicity of Zr–Nb alloys were investigated to explore their potential uses as new orthopedic implants. The alloying element Nb had significant influence on the microstructure of annealed Zr–Nb alloys. All the studied Zr–Nb alloys had a duplex structure of α and β phase and β phase increased with the increasing Nb content. The electrochemical corrosion performances of the Zr–Nb alloys were improved by the addition of Nb. The EIS data, fitted by $R_s(Q_pR_p)$, suggested a single passive film formed on metallic surface under the open-circuit condition. The association of values of corrosion current densities, passive current densities and pit potentials indicated that corrosion resistance increased with the increase of Nb content. The passive films of pure Zr and Zr–Nb alloys were the corrosion-resistant Nb and Zr oxides, which probably accounted for their excellent corrosion resistance. SEM of the corroded samples revealed that the alloys became more pit-resistant with the increase of Nb content. The results of cytotoxicity tests indicated that all studied Zr–Nb alloys exhibited excellent in vitro biocompatibility. All experimental results suggested that Zr–22Nb alloy showed the best electrochemical performance and good biocompatibility, thus making it a promising material for orthopedic devices.

Acknowledgments

References

[1] P. Thomsen, C. Larsson, L.E. Ericson, L. Sennerby, J. Lausmaa, B. Kasemo, J. Mater. Sci. Mater. Med. 8 (1997) 653–665.
[2] K.M. Sherepo, I.A. Red'ko, Biomed. Eng. 38 (2004) 77–79.
[3] E. Eisenbarth, D. Velten, M. Müller, R. Thull, J. Breme, Biomaterials 25 (2004) 5705–5713.
[4] A. Yamamoto, R. Honma, M. Sumita, J. Biomed. Mater. Res. 39 (1998) 331–340.
[5] O.B. Kulakov, A.A. Doktorov, S.V. Diakova, Y.I. Denisov-Nikolskiy, K.A. Grötz, Morfologiya 127 (2005) 52–55.
[6] M.B. Guglielmotti, S. Renou, R.L. Cabrini, Int. J. Oral Maxillofac. Implants 14 (1999) 565–570.
[7] L.W. Hobbs, V.B. Rosen, S.P. Mangin, M. Treska, G. Hunter, Int. J. Appl. Ceram. Technol. 2 (2005) 221–246.
[8] J.K.L. Lee, K. Maruthainar, N. Wardle, F. Haddad, G.W. Blunn, Knee 16 (2009) 269–274.
[9] H.C. Hsu, S.C. Wu, Y.C. Sung, W.F. Ho, J. Alloys Compd. 488 (2009) 279–283.
[10] S.N. Nomura, K. Oya, Y. Tanaka, R. Kondo, H. Doi, Y. Tsutsumi, T. Hanawa, Acta Biomater. 6 (2010) 1033–1038.
[11] M. Uchida, H.M. Kim, F. Miyaji, T. Kokubo, T. Nakamura, Biomaterials 23 (2002) 313–317.
[12] H. Tsuchiya, J.M. Macak, A. Ghicov, L. Taveira, P. Schmuki, Corros. Sci. 47 (2005) 3324–3335.
[13] L. Saldaña, A. Mendéz-Vilas, L. Jiang, M. Multigner, J.L. González-Carrasco, M.T. Pérez-Prado, M.L. González-Martin, L. Munuera, N. Vilaboa, Biomaterials 28 (2007) 4343–4354.
[14] L.V. Branzoi, M. Iordoc, M. Codescu, Surf. Interface Anal. 40 (2008) 167–173.
[15] N.T.C. Oliveira, S.R. Biaggio, R.C. Rocha-Filho, N. Bocchi, J. Biomed. Mater. Res. Part A 74 (2005) 397–407.
[16] N.T.C. Oliveira, S.R. Biaggio, R.C. Rocha-Filho, N. Bocchi, J. Braz. Chem. Soc. 13 (2002) 463–468.
[17] A.K. Satpati, S.V. Phadnis, R.I. Sundaresan, Corros. Sci. 47 (2005) 1445–1458.
[18] R. Tewari, D. Srivastava, G.K. Dey, J.K. Chakravarty, S. Banerjee, J. Nucl. Mater. 383 (2008) 153–171.
[19] T. Akahori, M. Niinomi, M. Nakai, H. Tsutsumi, T. Hattori, H. Fukui, Mater. Sci. Forum 638–642 (2010) 495–500.
[20] H. Okamoto, J. Phase Equilib. 13 (1992) 577.
[21] ISO-10993-5: Biological Evaluation of Medical Devices—Part 5: Test for In Vitro Cytotoxicity, ANSI/AAMI, Arlington, VA, 1999.
[22] Y.Z. Huang, D.J. Blackwood, Electrochim. Acta 51 (2005) 1099–1107.
[23] J.E.G. Gonzalez, J.C. Mirza-Rosca, J. Electroanal. Chem. 471 (1999) 109–115.
[24] A.K. Shukla, R. Balasubramaniam, S. Bhargava, Intermetallics 13 (2005) 631–637.
[25] D. Mareci, R. Chelariu, D.M. Gordin, G. Ungureanu, T. Gloriant, Acta Biomater. 5 (2009) 3625–3639.
[26] C.O.A. Olsson, D. Landolt, Corros. Sci. 46 (2004) 213–224.
[27] Y. Tanaka, M. Nakai, T. Akahori, M. Niinomi, Y. Tsutsumi, H. Doi, T. Hanawa, Corros. Sci. 50 (2008) 2111–2116.
[28] G.K. Dey, R.N. Singh, R. Tewari, D. Srivastava, S. Banerjee, J. Nucl. Mater. 224 (1995) 146–157.
[29] O.T. Woo, Y.P. Lin, J. Nucl. Mater. 270 (1999) 376–381.
[30] Y. Tsutsumi, Y. Takano, H. Doi, K. Noda, T. Hanawa, Mater. Sci. Forum 561–565 (2007) 1489–1492.
[31] G.C. Palit, H.S. Gadiyar, Corrosion 43 (1987) 140–148.
[32] G.C. Palit, K. Elayaperumal, Corros. Sci. 18 (1978) 169–179.
[33] X.N. Gu, Y.F. Zheng, Y. Cheng, S.P. Zhong, T.F. Xi, Biomaterials 30 (2009) 484–498.
[34] N.J. Hallab, S. Anderson, M. Caicedo, J.J. Jacobs, J. ASTM Int. 3 (2006) 429–440.
[35] G. Hunter, J. Dickinson, B. Herb, R. Graham, J. ASTM Int. 2 (2005) 409–422.
[36] L. Liu, C.L. Qiu, Q. Chen, K.C. Chan, S.M. Zhang, J. Biomed. Mater. Res. Part A 86 (2008) 160–169.
[37] Y.H. Yun, V.T. Turitto, K.P. Daigle, P. Kovacs, J.A. Davidson, S.M. Slack, J. Biomed. Mater. Res. 32 (1996) 77–85.